Research Article Vol. 2, No. 4 / April 2015 / Optica 313

Type I and II Bragg gratings made with infrared femtosecond radiation in high and low alumina content aluminosilicate optical fibers

Dan Grobnic,[1,*] Stephen J. Mihailov,[1] John Ballato,[2] and Peter D. Dragic[3]

[1]National Research Council of Canada, 100 Sussex Drive, Ottawa K1A 0R6, Canada

[2]Department of Materials Science and Engineering, Clemson University, Clemson, South Carolina 29634, USA

[3]University of Illinois at Urbana-Champaign, Urbana, Illinois 61801, USA

*Corresponding author: dan.grobnic@nrc-cnrc.gc.ca

Received 30 October 2014; revised 18 February 2015; accepted 19 February 2015 (Doc. ID 226024); published 30 March 2015

Aluminosilicate fibers have very low Brillouin scattering gain coefficients, making them interesting fibers for nonlinear optical applications. We manufactured Bragg gratings in high (30 mol.%) and low (4 mol.%) alumina content optical fiber using 800 nm femtosecond pulse duration radiation and a phase mask. Grating spectral characteristics and thermal behavior are presented. Index modulations $>10^{-3}$ were generated for fundamental pitched Bragg gratings, and $>10^{-4}$ for higher-order gratings. Gratings were annealed at temperatures up to 900°C. Type II gratings written in fibers with lower alumina content showed better thermal stability than gratings written in fibers with higher alumina content. Bragg gratings in these fibers would be well suited as laser cavity mirrors in high-energy laser systems, as well as in telecommunication and sensor systems where Brillouin scattering restricts power scaling.

OCIS codes: (060.3735) Fiber Bragg gratings; (060.7140) Ultrafast processes in fibers.

http://dx.doi.org/10.1364/OPTICA.2.000313

1. INTRODUCTION

Infrared (IR) femtosecond pulse duration (ultrafast) radiation can penetrate and induce changes in the refractive index of virtually any material that is transparent to low-signal-intensity IR radiation. This capability has opened the possibility for fiber Bragg grating (FBG) inscription [1] in a wide variety of waveguide material substrates with optical properties beyond those of the silica-based fibers that have been the staple of the UV Bragg grating fabrication industry [2]. Bragg grating structures have been reported in crystalline materials (lithium niobate, sapphire, and YAG) [3], glassy materials (chalcogenide, borosilicate, fluoride, and phosphate glasses [4]), and bismuth oxide fibers [5]. FBGs have been inscribed in active silica fibers co-doped with Er/Yb and low concentrations of Al to act as laser cavity mirrors for fiber lasers [6] and in-fiber temperature-sensing elements [7]. Such structures have been characterized and used in applications that require in-line Bragg gratings. Depending on the intensity of the beam within the waveguide, gratings can be written either in the type I regime below the ionization threshold through a multiphoton absorption process, or above the ionization threshold in the type II regime. In the latter case, index changes caused by avalanche ionization and plasma formation are permanent at temperatures approaching the glass transition temperature of the waveguide.

Recently, we presented the fabrication of FBGs in a new quasi-single-mode aluminosilicate optical fiber possessing an alumina content in excess of 30 mol.% using 800 nm femtosecond pulse duration radiation and a phase mask [8] where high index modulations $\Delta n > 10^{-3}$ were realized. More recently, FBG fabrication has been reported in a higher alumina content aluminosilicate optical fiber (49.4 mol.%) using 400 nm femtosecond pulse duration radiation and a Talbot

interferometer [9]. Highly multimode grating responses similar to those written in pure sapphire fiber rods [10] were realized, but with thermal stabilities lower than type II femtosecond laser-induced FBGs in silica-based fibers [2].

In this paper, we present the optical and thermal characteristics of Bragg gratings inscribed in high (30 mol.%) and low (4 mol.%) alumina content silica optical fiber and compare those results to similar gratings written in telecom standard single-mode Ge-doped silica fibers.

2. EXPERIMENTAL PROCEDURES

Fiber A, the high-concentration (~30 mol.%) alumina fiber, was fabricated using a sapphire precursor core, a silica glass sleeve, and the molten core approach for drawing the fiber [11]. It has a core diameter of about 30 μm and a 150 μm outer diameter cladding of pure silica [11]. It was characterized as having a very low Brillouin scattering gain coefficient. The measured loss of this fiber was about 0.2 dB/m in the near-IR spectral region, suggesting that scattering from either material phase separation or the core-clad interface were not problematic. Additional details on fiber fabrication and materials properties are provided in Ref. [11]. No other dopants aside from the crystalline sapphire rod and the fused silica sleeve preform combination are used. Fiber B has a lower alumina content of ~4 mol.%, 8 μm core, and 125 μm cladding diameter. It was fabricated using the modified chemical vapor deposition (MCVD) approach. The refractive index profiles of the fibers were measured at 980 nm (Interfibre Analysis) using a spatially resolved Fourier transform technique [12], and are shown in Fig. 1.

Gratings were fabricated in the two different aluminosilicate fibers. SMF-28 Ge-doped silica fiber was used to inscribe control gratings under similar conditions for comparison with the gratings inscribed in the aluminosilicate fibers.

A Coherent Libra regeneratively amplified femtosecond laser having 80 fs pulse duration and 7 mm beam diameter was used for the grating inscription. The laser was operated at 100 Hz repetition rate for type I grating inscription [13], 20 Hz for type II gratings in the high-content alumina fiber and, 5 Hz for type II grating in silica and low-content alumina fiber. The 1.5 mJ femtosecond pulses were focused through a 19 mm focal length cylindrical lens and a phase mask with different pitches, into the core of the fiber. The laser beam was scanned across the fiber by dithering the focusing lens using a piezo actuator with a ±10 μm amplitude in order to optimize the overlap of the grating structure with the grating core.

The fibers were placed in a fiber jig at 2 mm distance from the phase mask for the type I gratings and 0.5 mm for the type II gratings in order to promote two-beam and multiple-beam interference, respectively [13]. An ANDO optical spectrum analyzer was used to monitor the grating spectral behavior during the inscription process. The gratings were then remeasured using a high-resolution tunable laser spectral measurement system. The silica fiber and the low alumina content fiber were fusion spliced to connectorized pigtails and connected to the spectral measurement system. The cleaved ends of the high-content alumina fibers were placed on six-axis precision stages in order to "butt-to-butt" couple the probe light into the fiber samples while the fiber was located on the writing jig. Reflected or transmitted signals from the Bragg gratings were then extracted and fed into the spectral measurement system. The annealing tests were carried out in a Lindbergh tube furnace with temperature control up to 1200°C.

3. RESULTS AND DISCUSSION

A. Gratings in High Alumina Content Fiber (Fiber A)

Low zero-order phase masks optimized for the 800 nm radiation with pitches Λ of 3.21 and 3.14 μm were used to test the capability of the IR radiation to interact with the fiber. Very weak refractive index modulations Δn of about 10^{-6} were inscribed with pulse energies of 460 μJ. Assuming Gaussian beam optics and the absence of the fiber, this pulse energy corresponds to a peak intensity in the focal volume of the interference field pattern generated by the phase mask of $\sim 2 \times 10^{13}$ W/cm^2. This pulse energy is higher than the 300 μJ energy required to inscribe a grating of the same strength in silica fiber.

1.5 mJ/pulses were used to inscribe strong gratings. The grating growth was rapid (~10 s exposure) but seemed to saturate at about 3–5 dB strength (Fig. 2). Assuming Gaussian beam optics where the focal line width was calculated to be 2.76 μm and considering that the dithering duty cycle

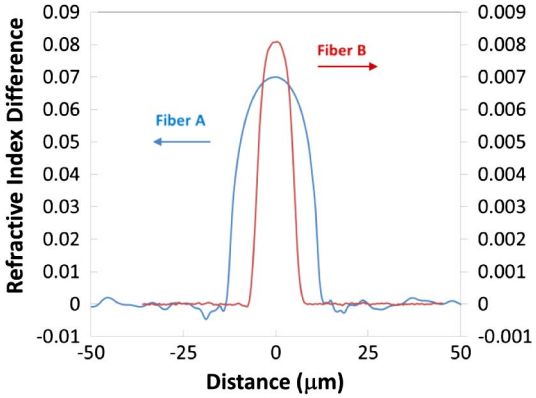

Fig. 1. Refractive index profiles of high-concentration Al Fiber A (blue) and low-concentration Al Fiber B (red).

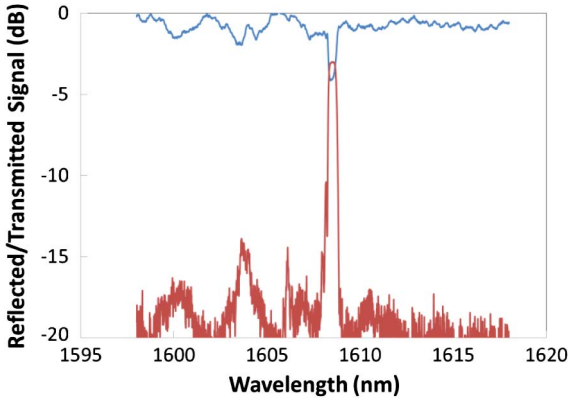

Fig. 2. Transmission (blue) and reflection (red) spectra of a grating made with a Λ = 3.21 μm phase mask in Fiber A.

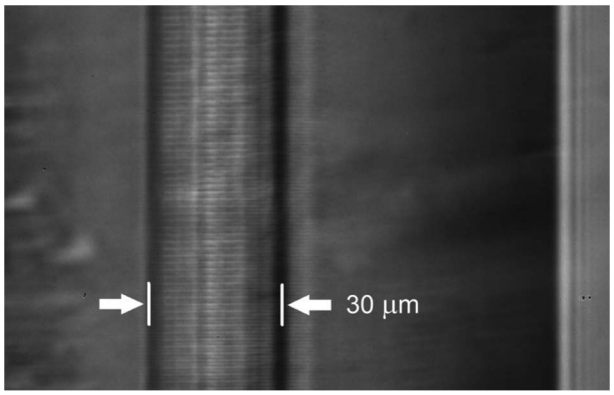

Fig. 3. Microscope image of the high-order grating made in Fiber A as viewed normal to the optical axis of the inscription beam.

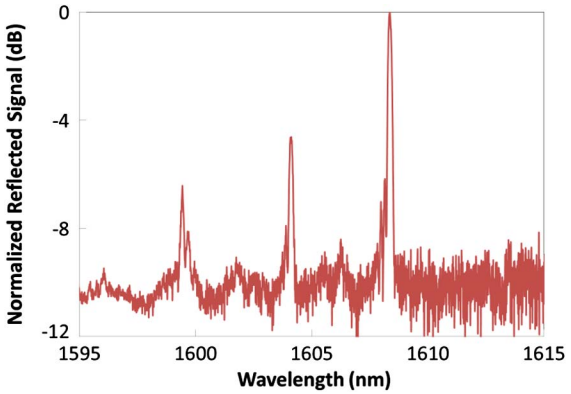

Fig. 4. Multimode grating structure (Fiber A) with fundamental Bragg resonance at 1608 nm.

duration was 20 seconds, the number of superimposed pulses/unit area to induce the saturated index change was 360. The same result was obtained using second-order phase masks with 2.14 μm pitch. As seen under an optical microscope using a 50× microscope objective (Fig. 3), the total grating length is about 5 mm. A 5 dB grating of this length would correspond to a $\Delta n = 2 \times 10^{-4}$ for a first-order grating. Since a third-order grating structure contains fewer grating planes than a first-order grating, the actual Δn of the gratings would be higher, approaching 10^{-3}. The low saturation limit of these gratings could be an indication of a limited capability of the aluminosilicate material to support large variations in the refractive index or a small high-order Fourier component [14].

According to the Bragg wavelength relation $m\lambda_{Br} = n_{eff}\Lambda$, where m is the order of the Bragg reflection, λ_{Br} is the Bragg resonance wavelength, and n_{eff} is the effective refractive index of the fundamental core mode, n_{eff} was calculated to be 1.503, which is significantly higher than the n_{eff} of silica telecom fibers (1.447 at 1550 nm). Multiple attempts to optimize the writing process did not result in larger reflectivity gratings when the high-order phase mask was used. Grating strength consistently saturated at about 3–5 dB strength. As can be seen from the reflection spectrum (red trace, Fig. 2) there are higher-order modes reflected by the structure due to the waveguide being only quasi-single-mode at the interrogating wavelength. Depending on the grating position in the core and the launching conditions of the probe light, a different number of higher-order modes could be excited, as shown in Fig. 4. The inscription conditions used for the grating presented in Fig. 4 are identical to those used for the grating presented in Fig. 2, with the exception of the energy/pulse being set for this test at 1.2 mJ. While the intention was to place the fiber at the same position in the interference field created by the lens-phase mask, errors up to 5 μm in the vertical and horizontal position are to be expected. Since the grating does not completely overlap the 30 μm core of the fiber, changes in the overlap integral of the grating structure with the fundamental and higher-order modes are possible. It was also observed that the strength of the higher orders could be influenced by a slight misalignment in the coupling between the SMF 28 probe fiber and the high-alumina fiber.

Since the high-order gratings require a strongly nonsinusoidal refractive index profile in order to possess a strong higher-order Bragg resonance, a phase mask producing a first-order fundamental Bragg resonance (1.07 μm pitch) was also used to inscribe the Bragg grating. When measured with the erbium broadband source and the spectrum analyzer, this grating appeared to saturate also at about −3 dB strength. The transmission profile was different, however, compared to the high-order gratings having a very broad spectral bandwidth, (red trace, Fig. 5) and a flat irregular profile at 3 dB loss. The broadband transmission profile could indicate a chirped grating structure or a low overlap of the core fundamental mode with the grating structure. The gratings were then remeasured with an L-band tunable laser measurement system. With this type of excitation, the grating spectral response possessed a much stronger reflectivity, with a high attenuation at the Bragg wavelength (blue trace, Fig. 5). Based on the simulation of a first-order grating, the Δn of these gratings was found to be in excess of 10^{-3}.

At telecom wavelengths, the high alumina content fiber is highly multimode, resulting in excitation of high-order guided modes when the 30 μm core is coupled to a standard SMF probe fiber. The appearance of the 3 dB saturation when probed with a broadband source (Fig. 5) is likely due to

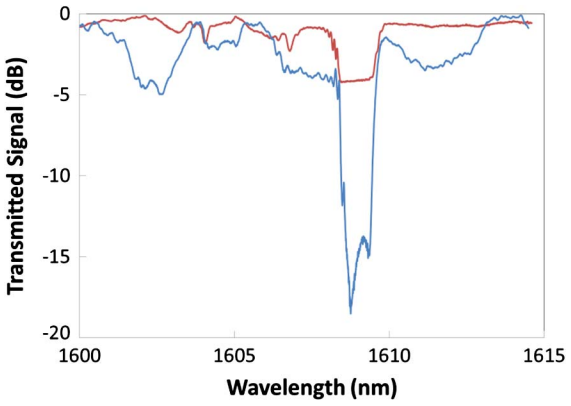

Fig. 5. Launching-condition-dependent transmission spectra: FBG made with $\Lambda = 1.07$ μm phase mask probed with an erbium white light source (red trace) and a tunable laser source (blue trace).

the propagation of these high-order modes around the grating, especially when one notes that the cross-section of the grating structure is less than the core diameter. When considering the ±10 μm sweep of the inscription beam and the total grating width when viewed normal to the optical axis of the inscription beam (Fig. 3), the cross-section of the grating is elliptical and centered on the core. It is possible, then, that the overlap of the grating with the polarized mode of the tunable laser is significantly larger than with the broadband source, resulting in a much larger reflectivity as observed in Fig. 5. The birefringence induced by the grating could also be a factor.

To test this hypothesis, in a separate experiment, a weak grating (~1% reflectivity) was written and probed with various states of polarization from a tunable laser source. When monitored in reflection, no variation in the Bragg wavelength was observed as a function of polarization, indicating that the fiber itself has low birefringence and a symmetric core. When a strong grating was written, however, strong polarization-dependent loss was observed.

This result indicated that larger refractive index changes can be induced in the aluminosilicate substrate, and that the early saturation of the high-order grating could be attributed to a quasi-sinusoidal index modulation profile of Bragg rather than a "top-hat" profile, which would contribute to strong high-order Fourier components of the grating structure [15]. This may be an indication of a different multiphoton absorption process in high alumina content glass compared to silica. While the bandgap for Ge-doped silica is evaluated to be 7.1 eV and seems to correspond to a 5 photon absorption process in Ge-doped silica [16], for alumina the bandgap was evaluated to be about 3 eV [17] and would correspond to a different absorption process and different profile of the refractive index modulation.

Inscription of type II gratings was also attempted in the high-content aluninosilicate fiber using writing parameters consistent with type II grating inscription in silica fibers. With this purpose in mind, a 3.21 and 1.07 μm pitched phase mask were used. The fiber was moved into close proximity with the phase mask (500 μm) to facilitate multiple beam interference that would produce an interference field with higher intensity than that created with pure two-beam interference, and is

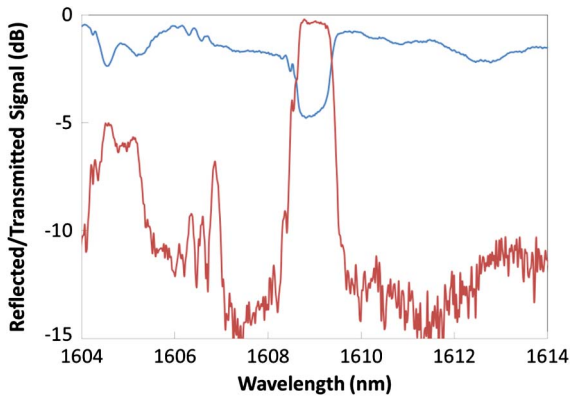

Fig. 6. Spectral characteristics of a type II grating made in high-content aluminosilicate fiber.

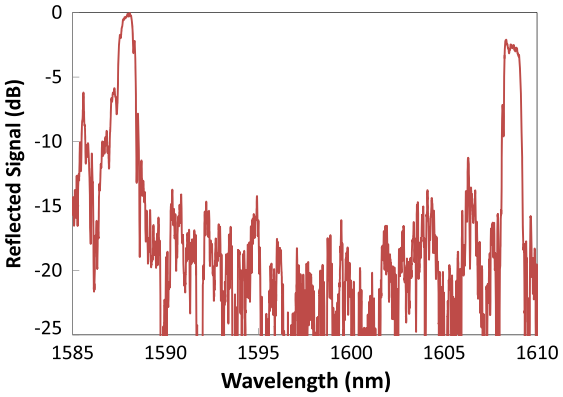

Fig. 7. Type II (left) and type I (right) gratings concatenated on the same strand of aluminosilicate fiber.

associated with the type II grating fabrication process. The fiber exposure resulted in a very strong grating (Fig. 6). Grating growth in aluminosilicate fibers written under these conditions was considerably faster than for the type I grating inscription described above, but slower when compared to gratings made under the same conditions in silica fiber, indicating a different absorption process in the aluminosilicate fiber as compared to that of silica.

Since the multimode nature of the aluminosilicate fiber makes it difficult to observe type II spectral characteristics of the grating (namely high coupling to cladding modes and high broadband loss), a saturated type I grating was first inscribed in the fiber and then a type II grating was written adjacent to the first grating (see Fig. 7).

The type I and the type II FBGs shown in Fig. 7 were inscribed with the parameters given in the experimental section. The phase mask producing a first-order grating (1.07 μm pitch) was used for the inscription of a type I FBG with a Bragg resonance of 1609 nm. The phase mask producing a third-order resonance (3.14 μm mask pitch) was used for the type II grating, resulting in a Bragg wavelength at 1588 nm. The type I grating was written first with the fiber placed 2 mm away from the mask to promote order walk-off and two-beam interference. The reflection spectrum was monitored during the inscription process until it saturated, indicating a near 100% reflectance. The first-order phase mask was then replaced with the third-order phase mask. The fiber and type I grating were then displaced parallel to the phase mask position such that the new type II grating would be written between the coupling point of the probe beam–aluminosilicate fiber and the type I grating. The 3.14 μm pitched mask was then placed at 500 μm distance from the fiber, after which the fiber was exposed to the fs radiation. During the inscription of the type II grating, it was observed that the measured reflectivity of the type I grating was reduced.

When the probe beam interacts first with the type II grating, the 1588 nm radiation is reflected by the first few grating planes of the structure because of the high refractive index modulation, resulting in no loss [18]. The 1609 nm radiation that passes through the type II grating is reflected 100% by the type I grating, but then passes again through the type II grating

on its way to the detector. The resulting difference of ~2 dB between the recorded reflection strength of the two 100% reflecting gratings indicates a loss of 1 dB of the 1609 nm radiation each time it passes through the type II grating. This large broadband loss is an indication of type II grating formation and was not observed when the gratings were inscribed with type I conditions.

B. Thermal Tests of Type II Gratings in High-Content Alumina Fiber

A number of type II gratings were isochronally annealed up to 800°C in ~200°C increments for one hour at each temperature to reach stabilization, while their spectra were monitored in reflection. Considering the polarization dependence of the spectral response, the grating reflection used for the estimation of the index modulation was measured using the broadband source. The annealing test demonstrates the grating endurance at high temperatures. Compared to type II silica gratings that have high stability at high temperature [19], the gratings made in our high-content alumina fiber decayed in a fashion similar to type I gratings made in silica (see Fig. 8). This result is different from the thermal stability of gratings reported in the 49.4 mol.% alumina content fiber, where induced Δn values remained stable up to 900°C [9].

The high-temperature annealing behavior indicates that either the defects formed or the high-content aluminosilicate substrate itself is not stable at elevated temperatures. Because there is immiscibility in the Al_2O_3–SiO_2 system for the compositions of these fibers [20], it is likely that the aluminosilicate cores will phase-separate above ~700°C for certain compositions and durations of temperature. For the high-content aluminosilicate data presented in Fig. 8, no appreciable insertion loss in the fiber was observed after one hour at 700°C. Given the intrinsic instability of the high aluminosilicate fiber composition, it is uncertain how long the gratings would last at this temperature.

The evaluation of the refractive index modulation of the gratings was made based on the reflection bandwidth and the assumption of ~3 mm long uniform gratings (as seen under the microscope). The multimode character of the fiber is of concern, as the overlap integral of the fundamental mode and the grating structure may change during the annealing process.

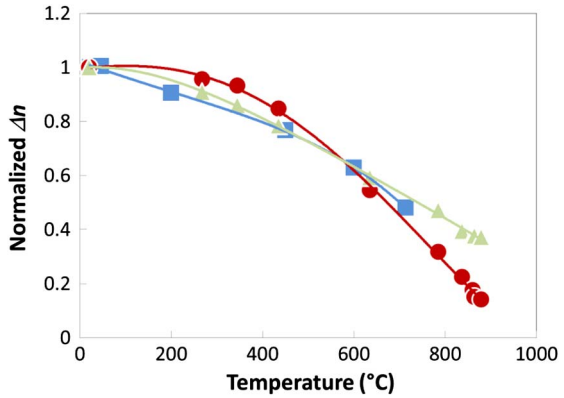

Fig. 8. Annealing characteristics of type I gratings made in silica fiber (green triangles), low-content aluminosilicate fiber (red circles), and type II gratings made in high-content aluminosilicate fiber (blue squares). Trend lines are shown to guide the eye.

The Bragg wavelength shift with the ambient temperature variation was measured to be 14.7 pm/°C, which is larger than 11 pm/°C for FBG shifts in silica fiber but smaller than the shifts for grating made in crystalline sapphire fibers (26 pm/°C) [21].

C. Bragg Grating Written in Low-Content Alumina Fiber (Fiber B).

A series of tests to inscribe type I and type II gratings were also made in a low alumina content aluminosilicate silica fiber. The inscription parameters presented in Section 2, including transversal scanning of the fiber core, were used to inscribe the type I grating in low-content alumina fiber and in SMF-28 fiber, with the exception of the pulse energy that was set at 1.2 mJ/pulse. Each of the gratings used for the annealing test presented in Fig. 8 were written with approximately 1000 laser pulses. The type I gratings made in this fiber were very similar in terms of energy threshold needed for grating formation as compared to silica fiber (280 μJ/pulse vs. 300 μJ/pulse, respectively); however, the growth rate in reflectivity of the grating was more rapid at higher pulse energies in the aluminosilica case. Various dopants and their concentrations in silica fibers can make the silica fiber more photosensitive to interactions with the IR ultrafast radiation [22].

The annealing behavior of the low alumina content aluminosilicate type I grating is similar to the type II grating presented previously in high-content alumina fibers and type I gratings made in SMF-28 fiber, although the gratings made in silica fiber tend to have higher stability at very high temperature (see Fig. 8).

Type II gratings were also inscribed in the low-content alumina fiber, using the same writing parameters for inscribing type II gratings in silica fiber as presented in Section 2 and using about 100 pulses for each grating. The resulting Bragg grating spectra possessed the type II spectral characteristic features of high cladding mode coupling and insertion loss. In order to better compare their high-temperature annealing behaviors, a 1 cm fiber was stripped and cleaved from each of the silica and low alumina content aluminosilicate fibers, then fusion spliced together. One grating was then written into the aluminosilicate side with a phase mask pitch of 1.0614 μm, and two superposed gratings were written on the silica fiber side with phase mask pitches of 1.0558 and 1.0682 μm. This created a Bragg resonance in the aluminosilicate grating of 1536.5 nm that was sandwiched in between the Bragg wavelengths of the two silica gratings, 1528.6 and 1544.4 nm, respectively (See Fig 9). From the Bragg resonance of 1536.5 nm and considering the mask pitch, the effective index of the low alumina content aluminosilicate fiber was determined to be 1.4478, which is very similar to that of the standard telecom Ge-doped silica fiber.

As can be seen in Fig. 10, the annealing behavior of the low-content aluminosilicate fiber grating is very similar to the gratings made in the silica fiber. At high temperature, the reflectivity of all the type II gratings increased, as the

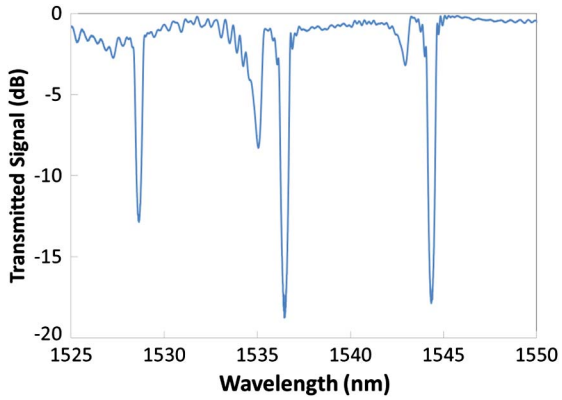

Fig. 9. Type II gratings in silica and low-content alumina fiber written in the spliced junction between the two fibers. The superposed gratings in the silica fiber have resonant wavelengths of 1528.6 and 1544.4 nm, while the low-content aluminosilicate fiber is resonant at 1536.5 nm.

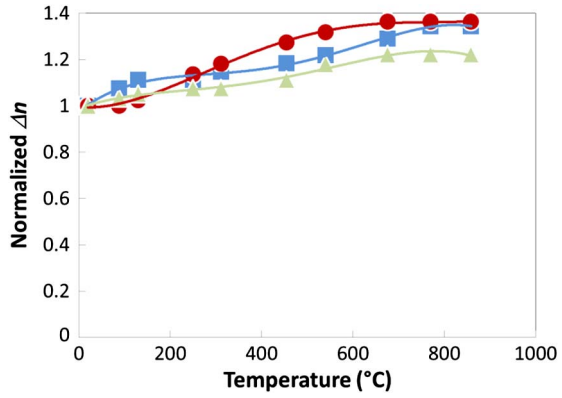

Fig. 10. High-temperature annealing of type II gratings made in low-content aluminosilicate fiber (blue squares) and silica fibers (red and green).

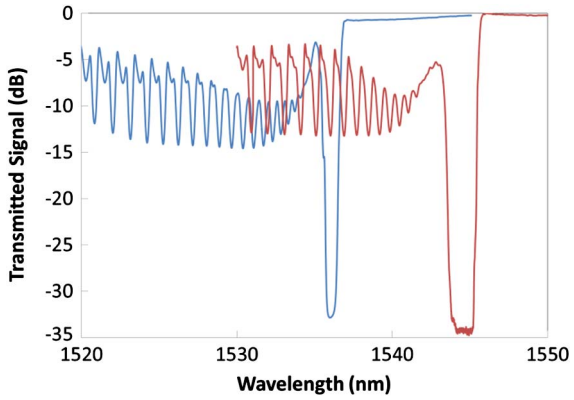

Fig. 11. Spectral transformation of a type II grating written in low-content aluminosilicate fiber from room temperature (blue) to 800°C (red).

annealable portion of refractive index change (type I) is erased. The resultant increase in grating strength with temperature on the low-content alumina fiber is presented in Fig. 11 for another grating written in low-content alumina fiber, where the transmission spectrum of the grating at room temperature is superposed with the spectrum of the same grating after 1 hour at 800°C. This transformation is permanent, being retained when the grating is cooled at room temperature.

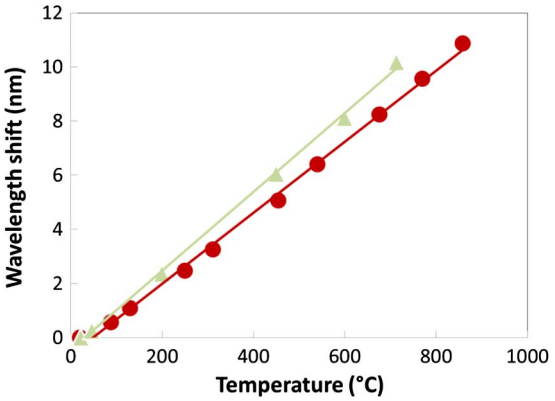

Fig. 12. Temperature shift of Bragg wavelength for type II gratings made in high alumina content (green triangle) and low alumina content (red circle) fibers.

The high and low alumina content fibers display slightly different sensitivities to the temperature, with the temperature coefficient at 14.7 pm/°C for the high-content fiber and 13.0 pm/°C for the low-content fiber (see Fig. 12). The reported 14.7 pm/°C is the average temperature sensitivity of the grating, resulting from a linear best fit of the experimental data in the temperature range from 22°C to 700°C. A quadratic interpolation of the wavelength shift versus temperature data indicates a ~13 pm/°C at room temperature and 14 pm/°C at 300°C. Both fibers have a quasi-linear dependency of the Bragg wavelength shift. These values are somewhat higher than the temperature coefficient of 12.4 pm/°C for the 49.4 mol.% alumina content fiber reported in [9].

4. MODELING THE TEMPERATURE SENSITIVITY

Conventional theoretical treatments of the sensitivity of fiber Bragg gratings to temperature and strain assume the physical properties of pure silica. This is reasonable considering that these conventional structures are fabricated in fibers composed mainly of silica. The silica approximation, however, breaks down in cases where a large quantity of it has been substituted by another material with different physical characteristics, such as in the high alumina content fibers of the present work. Such fibers instead require an alternative theoretical treatment that considers the physical characteristics of the multicomponent glass, including its constituents. From the measured data, it is clear that the aluminosilicate glass-based fiber gratings have a higher sensitivity to temperature than their mostly silica counterparts, but less than that of crystalline sapphire fiber [21]. The purpose of this section is, therefore, to explain the origins of this result utilizing a multicomponent glass approach. To begin modeling the temperature sensitivity of the Bragg wavelength, the derivative with respect to temperature of the Bragg equation is first found to be

$$\frac{d\lambda_{\text{Bragg}}}{dT} = \frac{1}{m}\left(\Lambda\frac{dn_{\text{eff}}}{dT} + n_{\text{eff}}\frac{d\Lambda}{dT}\right), \tag{1}$$

where the thermal dependence of the pitch Λ depends on the linear coefficient of thermal expansion (α_{CTE} or CTE) as

$$\frac{d\Lambda}{dT} = \Lambda\alpha_{\text{CTE}}. \tag{2}$$

Note that Eq. (1) is defined relative to the mask pitch. The in-fiber grating pitch will take on a value of $\Lambda/2$.

The thermo-optic coefficient dn_{eff}/dT is that of the optical mode in the fiber. To first order, however, the assumption is made that this value is simply that of the core material (the subscript '*eff*' will therefore subsequently be dropped), at large core-clad refractive index contrast. Furthermore, according to Prod'homme [23], dn/dT can be considered to be a combination of two physical phenomena. First, as the temperature is increased, thermal expansion and the commensurate change in mass density will result in a modified (decreased) refractive index. Second, as the material is heated, it acts as if in a state of increased dissociation, thereby resulting in a larger dipole moment (polarization) in the presence of an electromagnetic field. The former contribution to dn/dT requires that the core glass freely expand, but both processes mitigate each other, giving rise to thermo-optic coefficients that may be either positive or negative depending on which effect is stronger for a given material.

In the case of the aluminosilicate optical fiber, however, the core is clad rigidly in a material (pure silica) whose coefficient of thermal expansion (CTE) is much lower than that of the core [24]. This results in a reduction of the influence of the thermal expansion on the thermo-optic coefficient. In order to correct for this, first consider the likeness of the core, clad in a low-CTE material, to a freely expanding material undergoing compression to a smaller volume. Thus, one may liken the restricted thermal expansion to a negative strain in the axial direction and a negative tensile stress in the radial direction [24] of a free (unclad) material. This also mimics the effect of hydrostatic pressure: a contraction of an atom's electronic cloud, resulting in a decrease in the atomic polarizability [25]. Rather than attempting to distinguish these influences, the pressure-induced change in refractive index can instead be calculated via the photoelastic effect (i.e., the Pockels coefficients), giving rise to a correction to the thermally dependent refractive index. Stated more simply, the assumption is made that, with respect to refractive index, the fiber core freely expands with temperature, but a correction will be applied in the form of a negative strain to compensate for the much lower thermal expansion of the cladding.

To model the system, a simple unit volume of material is assumed with the geometry given in Fig. 13. First, assume an electromagnetic (EM) wave propagating in the z direction and polarized along the x direction. Any applied strain in the z direction will lead to a compression in the transverse directions governed by the Poisson ratio with

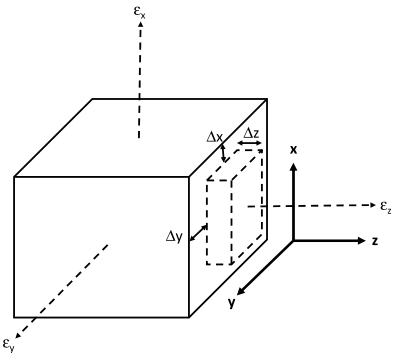

Fig. 13. Block diagram of a unit volume in the thermomechanical system.

$$\upsilon = -\frac{\varepsilon_x}{\varepsilon_z} = -\frac{\varepsilon_y}{\varepsilon_z}, \tag{3}$$

where ε is the fractional elongation, and as illustrated in Fig. 13. In this case, the change in refractive index as a function of strain may be written as [26]

$$\Delta n_x = -\frac{1}{2}n_{0,x}^3(p_{12} - \upsilon(p_{11} + p_{12}))\varepsilon_z, \tag{4}$$

where the subscript 0 implies the zero-strain, or relaxed, value and the subscript x refers to the EM wave polarization. In Eq. (4), the first appearance of p_{12} links the change in strain (along z) to the refractive index seen by the transversely polarized EM wave. The second term possessing the Poisson ratio υ links the resulting (transverse) compression (note the negative sign) to the index. One component of compression is in the same direction as the EM polarization and the other is transverse, leading to the presence of p_{11} and p_{12}, respectively, within the parentheses in Eq. (4).

Next, consider hypothetically that thermal expansion only occurs in the z direction. If thermal expansion were frustrated or prevented in that direction then, in accordance with Eq. (3), the material would tend instead to expand in the transverse directions. In this case, the change in refractive index would be identical in form as given in Eq. (4), but with the strain taking on a negative value. Whether the refractive index increases or decreases will depend on the sign of $p_{12} - \upsilon(p_{11} + p_{12})$.

Next, thermal expansion in the remaining two directions is considered. For restricted thermal expansion (negative strain) in the y direction, which is also transverse to the EM wave polarization, Eq. (4) is modified only slightly to account for this new direction of strain, giving

$$\Delta n_x = -\frac{1}{2}n_{0,x}^3(p_{12} - \upsilon(p_{11} + p_{12}))\varepsilon_y. \tag{5}$$

For strain in the x direction, which is in the same direction as the polarization, the change in index can be expressed as [26]

$$\Delta n_x = -\frac{1}{2} n_{0,x}^3 (p_{11} - 2\upsilon p_{12}) \varepsilon_x. \quad (6)$$

Here, the Poisson ratio links the change in index to the directions transverse to the strain, both of which are transverse to the polarization (and hence the factor of 2). The total change in refractive index then can be taken to be the sum of Eqs. (4), (5), and (6) since thermal expansion (and therefore negative strain) will occur in all directions. With the assumption of a uniform strain field throughout the material, $\varepsilon_x = \varepsilon_y = \varepsilon_z$ for an elevated temperature.

Next, in order to determine the correction to the refractive index, the change in index with pressure can be written in a chain rule formulation

$$\left.\frac{dn_x}{dT}\right|_{\text{correction}} = \frac{dn_x}{d\varepsilon}\frac{d\varepsilon}{dT}, \quad (7)$$

where

$$\frac{dn_x}{d\varepsilon} = -\frac{1}{2} n_{0,x}^3 [2(p_{12} - \upsilon(p_{11} + p_{12})) + (p_{11} - 2\upsilon p_{12})] \quad (8)$$

after summing Eqs. (4), (5), and (6) and assuming a uniform strain field. Equation (8) can be simplified and rewritten in alternate form, but this will not be done here as it is not an informative exercise. The change in strain (elongation) with temperature is the change in length that would have been observed in a freely expanding material, which is proportional to the linear CTE. Since the cladding does possess a non-zero CTE, one arrives at [24]

$$\frac{d\varepsilon}{dT} = -(\alpha_{\text{core}} - \alpha_{\text{clad}}), \quad (9)$$

with the presence of the negative sign to account for the negative strain due to restricted thermal expansion (effective compression). The subscripts in Eq. (9) refer to the core or cladding CTEs in the obvious way.

To model the grating system, the Bragg wavelength is first calculated as a function of temperature and then the slope of the thermal dependence is calculated. Starting with $\lambda_{\text{Bragg}}(T) = n(T)\Lambda(T)/m$, and considering Eq. (2), $\Lambda(T) = \Lambda(T = T_0)(\alpha_{\text{clad}}(T - T_0))$ is determined, where T_0 is some starting temperature (such as room temperature). Since the cladding (being significantly more voluminous than the core) restricts thermal expansion of the core, the pitch will increase with the CTE of the pure silica cladding, and not with that of the core. Then $n(T)$ is calculated utilizing the model in [27]. More specifically, the refractive index of the aluminosilicate glass is assumed to be additive in the alumina concentration ($[Al_2O_3]$ refers to the mole fraction of alumina) such that

$$n(T) = q n_A(T) + (1 - q) n_S(T), \quad (10)$$

where

$$q = \frac{\frac{M_{Al_2O_3}}{M_{SiO_2}} \rho_{SiO_2} [Al_2O_3]}{\rho_{Al_2O_3} + [Al_2O_3]\left(\frac{M_{Al_2O_3}}{M_{SiO_2}} \rho_{SiO_2} - \rho_{Al_2O_3}\right)}, \quad (11)$$

and where M is the molar mass and ρ is the mass density, with the subscripts utilized for the bulk constituents again in the obvious way. In Eq. (10), n_A refers to the refractive index of the alumina constituent and n_S to that of silica, and [after the correction, Eq. (7), is applied] each follows the form

$$n_{A,S}(T) = n_{0,A,S} + \frac{dn_{A,S}}{dT}(T - T_o) + \frac{dn_{A,S}}{d\varepsilon}\frac{d\varepsilon}{dT}(T - T_o). \quad (12)$$

In Eq. (12), dn/dT is the bulk (i.e., uncorrected) thermo-optic value (silica or alumina value), p_{11} *and* p_{12} [after substituting Eq. (8)] are the bulk values for silica or alumina, and the core CTEs are calculated for the *aggregate* glass since a uniformly distributed stress or strain is assumed within the core. This is calculated as

$$\alpha = q\alpha_A + (1 - q)\alpha_S. \quad (13)$$

Utilizing the materials values found in [28] (mass density, Poisson ratios, p_{11}, and p_{12} for both silica and alumina), [24] (CTEs), [8] (alumina refractive index), and [29] (dn/dT for silica and alumina), we obtain the result provided in Fig. 14 for a starting (mask) pitch (at $T = T_0$) of 3.27 μm and $m = 3$ (solid line). The physical values are reproduced in Table 1 as a courtesy to the reader. For this calculation, dispersion in n_0 has been neglected, but this introduces an insignificant error across the realized experimental wavelength range for λ_{Bragg}. Also shown in the figure are the two measurements from this work (from Fig. 12), the zero-alumina-content data point extrapolated from [30] utilizing their combined CTE and dn/dT value of 7.5×10^{-6} per Kelvin, the value found for a pure unclad sapphire fiber [21], and the value found in [9] at 50 mol.% of alumina.

For completeness, Fig. 14 also shows the modeling result for an unclad solid aluminosilicate fiber (dashed line). In this

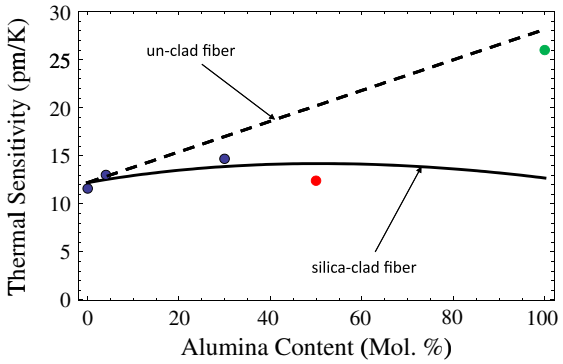

Fig. 14. Modeled temperature sensitivity of the type II gratings as a function of alumina content (solid line silica-clad fiber, dashed line un-clad fiber). The data points for the silica-clad aluminosilicate glass are from this work (Fig. 12), Ref. [9] (red dot), pure unclad sapphire fiber [21] (green dot), and the zero-alumina point is from [30].

Table 1. Summary of Physical Properties of the Various Glass Constituents

Value	SiO_2	Al_2O_3
Index (at 1534 nm)	1.444	1.653
Molar mass (g/mol)	60.08	101.96
Density ρ (kg/m^3)	2200	3350
dn/dt (10^{-6} K^{-1})	10.4	13.5
CTE (10^{-6} K^{-1})	0.54	7.7
p_{11}	0.098	−0.237
p_{12}	0.226	−0.027
Poisson Ratio	0.16	0.25

case, the CTE governs as $\Lambda(T) = \Lambda(T = T_0)(\alpha_{\text{core}}(T - T_0))$ and there is no strain correction to the refractive index, since there is no cladding. We see that the model overestimates the thermal sensitivity for pure alumina by about 10% relative to the measured data, suggesting that the CTE of alumina may be slightly lower than the value provided in Table 1.

The agreement between the model and experimental data is very good, given the level of uncertainty in the values provided in Table 1, and it is noted that the modeling itself is not a fit to the data. For example, it is known that the mass density of alumina within the glass matrix will influence the slope of the curve [29], and also that the mass density will, in turn, influence the refractive index, with both of these being a function of fiber fabrication conditions. Furthermore, the CTEs are taken from fibers derived from glasses fabricated using alternative processes, and an error in the CTE of alumina will alter the curvature in Fig. 14. However, regardless of these issues, the conclusion may be drawn that the increased sensitivity to temperature of the Bragg wavelength (up to about 60 mol.% of alumina) results from the relatively large CTE of the aluminosilicate core which is offset by the binding effect of the cladding that introduces a negative strain on the core. Interestingly, in the present case, this net enhancement in sensitivity appears to be significantly weaker in the silica-clad material than in a freely expanding material (such as unclad pure crystalline sapphire). As such, gratings produced in unclad pure sapphire have a somewhat stronger thermal sensitivity than those (extrapolated) in silica-clad pure alumina (26 versus about 12.5 pm/K). For all practical purposes, aluminosilicate-core fibers clad in silica appear to have sensitivities that are very similar to (but slightly higher than) other silica-clad fibers with mainly silica cores. In the case of a core material with large CTE, increased thermal sensitivity would be gained through the use of a cladding material with CTE larger than that of silica.

5. CONCLUSIONS

Using femtosecond IR radiation and the phase mask method, type I and type II gratings with fundamental and high-order Bragg resonances have been written in high and low alumina content aluminosilicate fibers. Refractive index modulations in excess of 10^{-3} have been obtained. The low-content alumina fiber behaves in a similar fashion to silica fiber. The slightly lower grating inscription energy threshold and higher grating growth rate for the low alumina content fiber are also consistent with the inscription behavior of silica fiber doped with other elements like erbium.

The high-content alumina fiber shows a very different behavior with respect to gratings inscription and its interaction with the ultrafast laser field, as well as with the optical and thermal properties of the grating. There are indications that the refractive index modulation of type I gratings in high-content alumina fiber are closer to a sinusoidal profile than that generated by the ultrafast interference field in the silica fiber. Type II gratings in this fiber are not stable at high temperature, indicating that the multiphoton ionization process does not result in a high-temperature-stable material or stress-induced refractive index changes. Alternatively, the phase transition of the fiber is very low. It was observed that the temperature sensitivity of the fiber, 14.7 pm/°C, is larger than that of silica fiber (10–12) pm/°C at low to moderate temperatures.

REFERENCES

1. S. J. Mihailov, C. W. Smelser, P. Lu, R. B. Walker, H. Ding, D. Grobnic, G. Henderson, and J. Unruh, "Fiber Bragg gratings made with a phase mask and 800-nm femtosecond radiation," Opt. Lett. **28**, 995–997 (2003).
2. S. J. Mihailov, D. Grobnic, C. W. Smelser, P. Lu, R. B. Walker, and H. Ding, "Bragg grating inscription in various optical fibers with femtosecond infrared lasers and a phase mask," Opt. Mater. Express **1**, 754–765 (2011).
3. D. Grobnic, S. J. Mihailov, and C. W. Smelser, "Bragg gratings made with ultrafast radiation in crystal waveguides, lithium niobate, sapphire and YAG Bragg gratings," Proc. SPIE **6796**, 679620 (2007).
4. D. Grobnic, S. J. Mihailov, C. W. Smelser, and R. B. Walker, "Bragg gratings made with ultrafast radiation in non-silica glasses; fluoride, phosphate, borosilicate and chalcogenide Bragg gratings," Proc. SPIE **6796**, 67961K (2007).
5. D. Grobnic, R. B. Walker, S. J. Mihailov, C. W. Smelser, and P. Lu, "Bragg gratings made in highly nonlinear bismuth oxide fibers with ultrafast IR radiation," IEEE Photon. Technol. Lett. **22**, 124–126 (2010).
6. E. Wikszak, J. Thomas, J. Burghoff, B. Ortaç, J. Limpert, S. Nolte, U. Fuchs, and A. Tünnermann, "Erbium fiber laser based on intracore femtosecond-written fiber Bragg grating," Opt. Lett. **31**, 2390–2392 (2006).
7. M. Leich, J. Fiebrandt, A. Schwuchow, S. Unger, S. Jetschke, and H. Bartelt, "Femtosecond pulse-induced fiber Bragg gratings for in-core temperature measurement in optically pumped Yb-doped silica fibers," Opt. Commun. **285**, 4387–4390 (2012).
8. D. Grobnic, S. J. Mihailov, J. Ballato, and P. Dragic, "Bragg gratings made with IR femtosecond radiation in high alumina content aluminosilicate optical fibers," in *Advanced Photonics*, OSA Technical Digest Series (Optical Society of America, 2014), paper BW2D.4.
9. T. Elsmann, A. Lorenz, N. S. Yazd, T. Habisreuther, J. Dellith, A. Schwuchow, J. Bierlich, K. Schuster, M. Rothhardt, L. Kido, and H. Bartlet, "High temperature sensing with fiber Bragg gratings in sapphire-derived all-glass optical fibers," Opt. Express **22**, 26825–26833 (2014).
10. D. Grobnic, S. J. Mihailov, C. W. Smelser, and H. Ding, "Sapphire fiber Bragg grating sensor made using femtosecond laser radiation for ultrahigh temperature applications," IEEE Photon. Technol. Lett. **16**, 2505–2507 (2004).
11. P. Dragic, T. Hawkins, P. Foy, S. Morris, and J. Ballato, "Sapphire-derived all-glass optical fibers," Nat. Photonics **6**, 629–635 (2012).
12. A. Yablon, "Multi-wavelength optical fibre refractive index profiling by spatially resolved Fourier transform spectroscopy," J. Lightwave Technol. **28**, 360–364 (2010).

13. C. W. Smelser, S. J. Mihailov, and D. Grobnic, "Formation of type I-IR and type II-IR gratings with an ultrafast IR laser and a phase mask," Opt. Express **13**, 5377–5386 (2005).
14. C. W. Smelser, S. J. Mihailov, and D. Grobnic, "Characterization of Fourier components in type I infrared ultrafast laser induced fiber Bragg gratings," Opt. Lett. **32**, 1453–1455 (2007).
15. C. W. Smelser, S. J. Mihailov, and D. Grobnic, "Impact of index change saturation on the growth behavior of higher-order type I ultrafast induced fiber Bragg gratings," J. Opt. Soc. Am. B **25**, 877–883 (2008).
16. J. Nishii, N. Kitamura, H. Yamanaka, H. Hosono, and H. Kawazoe, "Ultraviolet-radiation induced chemical reactions through one- and two- photon absorption processes in GeO_2-SiO_2 glasses," Opt. Lett. **20**, 1184–1186 (1995).
17. V. Rose and R. Franchy, "The band gap of ultrathin amorphous and well-ordered Al_2O_3 films on CoAl(100) measured by scanning tunneling spectroscopy," J. Appl. Phys. **105**, 07C902 (2009).
18. D. Grobnic, S. J. Mihailov, R. B. Walker, and C. W. Smelser, "Reflection characteristics of type II FBG made with femtosecond radiation," in *Bragg Gratings, Photosensitivity and Poling in Glass Waveguides (BGPP)*, Colorado Springs, CO, June 17–20 2012, paper BM2D.5.
19. D. Grobnic, C. W. Smelser, S. J. Mihailov, and R. B. Walker, "Long-term thermal stability tests at 1000°C of silica fibre Bragg gratings made with ultrafast laser radiation," Meas. Sci. Technol. **17**, 1009–1013 (2006).
20. T. Takamori and R. Roy, "Rapid crystallization of SiO_2–Al_2O_3 glasses," J. Am. Ceram. Soc. **56**, 639–644 (1973).
21. D. Grobnic, S. J. Mihailov, H. Ding, F. Bilodeau, and C. W. Smelser, "Single and low order mode interrogation of a multimode sapphire fibre Bragg grating sensor with tapered fibres," Meas. Sci. Technol. **17**, 980–984 (2006).
22. S. J. Mihailov, D. Grobnic, C. W. Smelser, P. Lu, R. B. Walker, and H. Ding, "Induced Bragg gratings in optical fibers and waveguides using an ultrafast infrared laser and a phase mask," Laser Chem. **2008**, 1–20 (2008).
23. L. Prod'homme, "A new approach to the thermal change in the refractive index of glasses," Phys. Chem. Glasses **1**, 119–122 (1960).
24. P. D. Dragic, C. Kucera, J. Ballato, D. Litzkendorf, J. Dellith, and K. Schuster, "Brillouin scattering properties of lanthano-aluminosilicate optical fiber," Appl. Opt. **53**, 5660–5671 (2014).
25. R. M. Waxler and G. W. Cleek, "The effect of temperature and pressure on the refractive index of some oxide glasses," J. Res. Natl. Bur. Stand. A **7A**, 755–763 (1973).
26. M. Huang, "Stress effects on the performance of optical waveguides," Int. J. Solids Struct. **40**, 1615–1632 (2003).
27. J. Ballato and P. Dragic, "Rethinking optical fiber: new demands, old glasses," J. Am. Ceram. Soc. **96**, 2675–2692 (2013).
28. P. D. Dragic, J. Ballato, S. Morris, and T. Hawkins, "Pockels' coefficients of alumina in aluminosilicate optical fiber," J. Opt. Soc. Am. B **30**, 244–250 (2013).
29. P. Dragic, J. Ballato, A. Ballato, S. Morris, T. Hawkins, P.-C. Law, S. Ghosh, and M. C. Paul, "Mass density and the Brillouin spectroscopy of aluminosilicate optical fibers," Opt. Mater. Express **2**, 1641–1654 (2012).
30. S. Magne, S. Rougeault, M. Vilela, and P. Ferdinand, "State-of-strain evaluation with fiber Bragg grating rosettes: application to discrimination between strain and temperature effects in fiber sensors," Appl. Opt. **36**, 9437–9447 (1997).